Two-step electrodeposition of Hausmannite sulphur reduced graphene oxide and cobalt-nickel layered double hydroxide heterostructure for high-performance supercapacitor

Gift Rutavi, Delvina Japhet Tarimo, Vusani Muswa Maphiri, Ncholu Manyala*

Department of Physics, Institute of Applied Materials, SARChI in Carbon Technology and Materials, University of Pretoria 0028, South Africa

*Corresponding author's email: ncholu.manyala@up.ac.za, Tel.: + (27)12 420 3549.

Abstract

Hausmannite /sulphur reduced graphene oxide (MO/RGO-S) and cobalt-nickel layered double hydroxide (CN) composite was synthesized through a two-step electrodeposition approach. This process began with galvanostatic electrodeposition of Hausmannite /sulphur reduced graphene oxide (MO/RGO-S) on a nickel foam (NF), followed by cyclic voltammetry (CV) electrodeposition of cobalt-nickel layered double hydroxide (CN). The inclusion of RGO-S increases the electrical conductivity of the active material (AM) and its wettability while Mn_3O_4 (MO) enhances the pseudocapacitive active sites which help to increase the specific capacity of CN. The materials' electrochemical evaluations were carried out via three- and two-electrode configurations using 2 M KOH electrolyte. An enhanced composite material (MO/RGO-S-50@CN) produced a phenomenal specific capacity of 582.1 mA h g^{-1} in a three-electrode configuration at 0.5 A g^{-1}. The device (MO/RGO-S-50@CN//CCBW) consisting of MO/RGO-S-50@CN and activated carbon from cooked chicken bone waste (CCBW) as positive and negative electrodes respectively delivered specific energy of 56.0 Wh kg^{-1} with a specific power of 515.0 W kg^{-1} at a specific current of 0.5 A g^{-1}. The device produced capacity retention of 85.1% and coulombic efficiency of 99.7 % at 10 000 galvanostatic charge-discharges (GCD) cycles at 6 A g^{-1}.

Because of these excellent results, the fabricated materials demonstrated great potential for application as high specific energy supercapacitor

Keywords: Layered double hydroxide; Energy storage; Spinels; Specific capacity; Hybrid capacitor.

1.0 Introduction

There are rising concerns over problems caused by the continued use of fossil fuels as an energy source. This is because of the pressure exerted on the environment and the depletion of fossil fuels. The intermittent nature of renewable sources of energy and the insufficient energy they produce is hampering the transformation from non-renewable to safer renewable energy sources [1]. From this background, it is essential to channel resources in researching on improving storage devices for renewable energy. Supercapacitors have been proven to have a very important contribution to renewable energy storage. This is because they possess some more favourable properties compared to batteries and fuel cells such as larger specific power, more rapid charge-discharge, longer cyclic life and they are more environmentally benign [2,3]. Supercapacitors are classified into pseudocapacitors (PS), electric double-layer capacitors (EDLC) and battery-type capacitors[4]. Battery-type capacitors and pseudocapacitors have become very popular in energy- storage, because of their reversible and rapid redox reactions at the electrolyte-electrode interface leading to very high theoretical specific capacities [5].

Transitional metal hydroxides (TMOH) which include $Co(OH)_2$ and $Ni(OH)_2$ are commonly utilised as battery-type materials owing to their low costs and abundant natural reserves [6,7]. However, these TMOH possess experimental capacities which are much less than their

theoretical capacities. This is due to very low intrinsic electrical conductivities (≈10^{-5} to 10^{-8} S.cm^{-1}) and limited diffusion pathways [8]. Hybrid hydroxides can alleviate this problem due to the synergistic effect of multiple components of materials consisting of more than one TMOHs such as layered double hydroxides (LDHs).

LDHs are inorganic, brucite-like materials with interlaminar anion between TMOH layers. The structure of LDH is $[M_{1-x}^{2+} M_x^{3+}(OH)_2]^{x+}(A^{n-})_{\frac{x}{n}}.mH_2O$, where M^{3+} and M^{2+} are trivalent and divalent metals respectively, x =M^{3+}/(M^{2+}+M^{3+}) is the proportion of the divalent metal M^{3+} and also the layer charge density, A^{n-} is the interlaminar organic or inorganic anion to balance the charges. This unique structure leads to high anion exchange capacity and tunable chemical composition which makes them suitable for use in supercapacitors [9–12]. LDHs which possess a 2D structure, are better alternatives to TMOHs as they exhibit larger theoretical specific surface area and possess many redox-active sites which enhance ion exchange and intercalation, promote redox reactions, flexible ion interchangeability and increase the number of structural defects [13].

Several methods have been utilised to synthesise LDHs, these include, electrodeposition, microwave-assisted synthesis, co-precipitation and solvothermal synthesis [14,15]. Electrodeposition is a more favourable method for the synthesis of LDHs. This is due to attributes such as low cost and efficient utilisation of active materials, morphology control, absence of binders, and strong adhesive forces between AM and the current collector (substrate). These properties endow electrodeposited LDHs with a larger specific capacity, higher rate capability and cyclic stability [16,17].

LDHs, however, suffer from low electrical conductivity, low cyclic performance, aggregation, poor electrochemical stability and poor rate capability due to slow reaction kinetics at high specific currents when performing charge-discharge processes [18,19]. This can be alleviated by producing a highly conductive and more stable heterostructure system with spinels configuration [20]. Spinels, which possess chemical structure MM'_2O_4, with M and M′ as divalent and trivalent metals respectively benefit from having high electrochemical activity due to reversible adsorption characteristics, multivalent charge transport, elevated chemical stability and increased redox reactions, these attributes increase the theoretical specific capacity. This is as a result of the improvement of electron transport efficiency and ion diffusion ratio [21,22]. The composite will benefit from the synergistic effect of different properties mentioned above and hence deliver a very high specific capacity.

Mn_3O_4 (Hausmannite) is one of the spinels structure that has been researched intensively as an electrode due to several favourable attributes which include large theoretical capacitance (1370 F g^{-1}) [23], wide range of active oxidation states, environmental safety, stable potential window in aqueous electrolyte and an outstanding Jahn-Teller effect [24,25]. However, it suffers from low electrical conductivity which reduces its performance. This can be improved by making a composite with functionalized carbon materials. Sulphur reduced graphene oxide (RGO-S) is one of the most favourable among the functionalized carbon materials because of the high electrical conductivity, enhanced redox-active sites, stability and excellent wettability with electrolyte ions [26].

The objectives of this study are to utilise a binder-free method to synthesize a composite electrode with three different types of materials, to perform structural and electrochemical characterisation of the composite and to incorporate it into the electrode for supercapacitor

device. Only a few studies have reported the combination of cobalt-nickel layered double hydroxide and Hausmannite spinel for supercapacitor applications. In this study, we are reporting for the first time the combination of cobalt-nickel layered double hydroxide, hausmannite spinel and carbon material through a binder-free and conductive additive-free synthesis route for supercapacitor applications. Also, the method is simple, safe and cost-effective as it is carried out at room temperature and atmospheric pressure and only very little material is lost during synthesis.

We are hereby reporting a two-step electrodeposition synthesis method to synthesise MO/RGO-S-X@CN heterostructure as a positive supercapacitor electrode where X denotes various masses in mg of RGO-S in the composite. MO/RGO-S-50@CN electrode produced the highest electrochemical attributes with an excellent specific capacity of 582.1 mAh g^{-1} at a specific current of 0.5 A g^{-1} in a three-electrode set up ahead of other composites. Furthermore, this electrode presented capacity retention of 86.5% and a coulombic efficiency of 99.9% after 5000 GCD cycles at 6 A g^{-1}. An asymmetric device was constructed by employing MO/RGO-S-50@CN as a positive electrode with CCBW as the negative electrode. This device MO/RGO-S-50@CN//CCBW produced specific energy of 56.0 Wh kg^{-1} at a specific current of 0.5 A g^{-1} with a specific power of 515.0 W kg^{-1}. The device also produced a coulombic efficiency of 99.7 % after 10 000 GCD cycles at 6 A g^{-1}. This study presents a novel approach of combining multiple electrode materials with different energy storage mechanisms by utilising just one simple binder-free method to produce excellent performance electrodes which are suitable contenders for high specific energy and power supercapacitor devices.

2.0 Experimental section

2.1 Materials

Only analytic quality chemicals were used in this research and no further processing of the chemicals was involved. These are the chemicals and materials used: Nickel foam [NF] purchased from Alantum (Munich, Germany). Ethanol [$CH_3\ CH_2OH$], Acetone [$(CH_3)_2\ CO$], and hydrochloric acid [HCl] were bought from (Sigma Aldrich, Steinheim, Germany). Nickel nitrate hexahydrate [$Ni\ (NO_3)_2 \bullet 6H_2O$], Cobalt nitrate hexahydrate [$Co(NO_3)_2 \bullet 6H_2O$], Sodium sulphate [Na_2SO_4], Manganese acetate hexahydrate [$Mn(CH_3COO)_2 \bullet 4H_2O$], Sulphur, and Sodium sulphide [Na_2S] were supplied from Merck (Johannesburg, South Africa). Deionised water (DW) was obtained using a DRAWELL purification machine.

2.2 Preparation of NF substrates

NF (1 cm × 2 cm) pieces were thoroughly treated by immersing in 4 M HCl, acetone, followed by absolute ethanol and finally deionised water, each for 20 minutes. The treated pieces were left to dry in an oven at 60^o C for 12 hours. This procedure was done because nickel metal is susceptible to forming inert oxide or hydroxide layer in a humid environment.

Synthesis of CN on NF

0.01 M of each $Co\ (NO_3)_2 \bullet 6H_2O$ and $Ni\ (NO_3)_2 \bullet 6H_2O$ were immersed in 50 ml of DW and stirred vigorously for 30 minutes to form the solution. Electrodeposition of CN on NF was performed via the 3-electrode set-up using the Bio Logic VMP 300 workstation (Knoxville, USA) controlled by EC-Lab V11.33 (Edmonton, AB, Canada). The working electrode (WE) was pre-treated NF while platinum wire and Ag/AgCl served as the counter electrode (CE) and reference electrode (RE) respectively. Cyclic voltammetry (CV) was carried out at a

scan rate of 5 mV s^{-1} for 3 cycles within a potential range -1.2 up to 0.5 V to deposit CN. The sample was then rinsed in DW and left to dry at 60 ℃ for 12 hours. The procedure was repeated for 6 and 9 CV cycles. The samples were labelled as CN-3, CN-6 and CN-9 where the number refers to the number of CV scan cycles.

2.4 Synthesis of MO/RGO-S composite on NF

Sulphur reduced graphene oxide (RGO-S) was produced using the procedure conveyed in our previous work [27]. 25 mg of RGO-S was then sonicated in DI water for 12 hours. Electrodeposition of MO/RGO-S on NF was performed via 3-electrode set-up using the Bio-Logic VMP-300 at room temperature. A solution was prepared by dissolving 0.16 M of Mn $(CH_3COO)_2$•$4H_2O$ and 0.16 M of Na_2SO_4 into 200 ml of DI water containing 25 mg RGO-S then stirring for 45 minutes. Na_2SO_4 served as a morphology directing agent and also helped minimise particle aggregation [28]. The RE and CE were as reported in section 2.3. The Mn_3O_4/RGO-S was grown using the galvanostatic electrodeposition method at 5 mA cm^{-2} for 30 minutes. Mn_3O_4/RGO-S on NF was then washed in DW and dried up at 80 ℃ for 5 hours. The deposition process was repeated by changing the mass of RGO-S in the solution. The samples were labelled MO (i.e., Mn_3O_4 without RGO-S) and MO/RGO-S-25, MO/RGO-S-50, and MO/RGO-S-75 according to the mass of RGO-S in the solution and the mass loading of the material on NF was 0.9, 1.1, 1.0, and 1.2 mg, respectively.

2.5 Synthesis of CN on MO/RGO-S

The electrodeposition process followed the same procedure in section 2.3 but with MO as the WE instead of NF and 6 CV cycles were used because CN-6 produced superior electrochemical results. The procedure was also repeated with the samples produced in

section 2.4 as MO/RGO-S-25, MO/RGO-S-50, and MO/RGO-S-75 as the WE. The samples were labelled MO@CN, MO/RGO-S-25@CN, MO/RGO-S-50@CN, and MO/RGO-S-75@CN with the total mass loading of the electrode's materials on NF as 1.0, 1.9, 2.1, 2.0, and 2.1 mg, respectively.

.

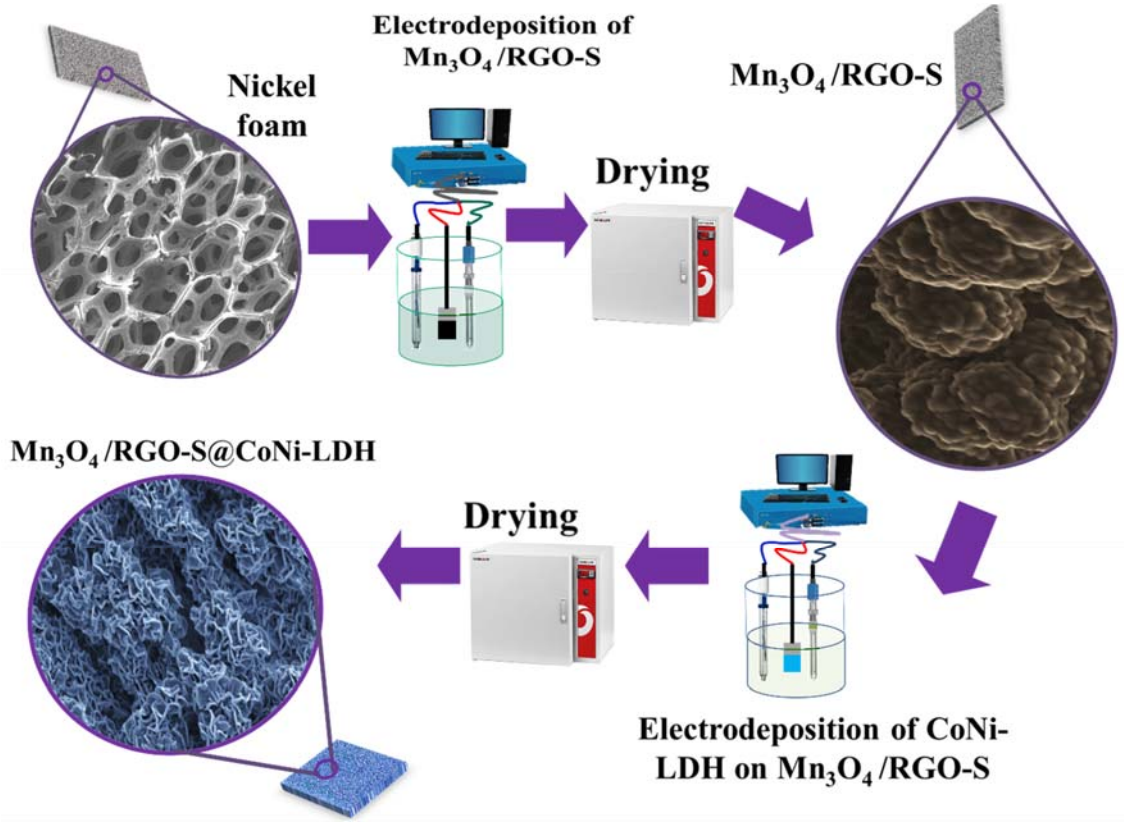

Fig. 1: Schematic illustration of the synthesis of Mn_3O_4/RGO-S@CN electrode.

2.6 Synthesis of cooked chicken bone waste (CCBW)

The activated carbon from cooked chicken bone waste (CCBW) was synthesized as follows: The CCBW were cleaned with ethanol then left to dry at 60 °C in the oven for 24 h. 5 g of the bones were pre-carbonized at 400 °C for 4 h using argon gas (200 sccm in a flow rate of

5 °C/min) to remove volatile particles and impurities. Subsequently, the pre-carbonized material was mixed with potassium hydroxide (weight ratio of 1:1) as an activating agent in the agitate motor followed by the addition of a few drops of DW to form a compacted block-like structure which was dried up at 100 °C for 12 h. Thereafter, the mixture was carbonized at 700 °C for 2 h in an argon environment (300 sccm at 5 °C/min). The attained sample was treated with 3 M HCl and washed with DW until neutrality was attained in the pH scale. The obtained sample was dried up for 24 h in an oven at 60 °C.

2.7 Material characterisation

The electrodeposition of MO/RGO-S as displayed in Fig. 1 began with the reduction of the acetate anions (CH_3COO^-) to acetic acid (CH_3COOH) at the cathode. This introduces hydroxyl anions (OH^-) into the sodium sulphate electrolyte. This leads to the deposition of manganese hydroxide on the nickel foam anode, which is then oxidised to Mn_3O_4 in the air. The GO-S nanorods are absorbed within the Mn_3O_4 matrix. The process is summarised by equation (1) - (3):

$$CH_3COO^- + H_2O \rightarrow CH_3COOH + OH^- \quad (1)$$

$$Mn^{2+} + 2OH^- \rightarrow Mn(OH)_2 \quad (2)$$

$$6Mn(OH)_2 + O_2 \rightarrow 2Mn_3O_4 + 6H_2O \quad (3)$$

For the electrodeposition of CN on MO/RGO-S, the process commences with the reduction of nitrate anions at the cathode. This produces hydroxyl anions for the oxidation of cobalt cation to form CN as shown in equations (4) and (5) below:

$$NO_3^- + H_2O + 2e^- \rightarrow NO_2^- + 2OH^- \quad (4)$$

$$Ni^{2+} + 2Co^{2+} + 6OH^{-1} \rightarrow NiCo_2(OH)_6 \quad (5)$$

X-Ray Diffraction (XRD) was employed to evaluate the samples' structure, The instrument incorporates a diffractometer (Brucker 2D PAN analytical BV, Amsterdam, Netherlands), operating with Cu $K_{\alpha 1}$ (λ = 0.154061 nm) at 2θ values 5- 90^o with intervals of 0.05^o. Raman spectroscopy measurements were carried out by employing a WITec Confocal Raman microscopy (WITec alpha-300R, Ulm Germany) with a 532 nm laser, spectral acquisition of 120s using a 50X objective. The morphology of CN and MO/RGO-S@CN were acquired using a Zeiss Ultra PLUS FEG-SEM (Ashikima Shi, Japan) at 2,000 V incorporating the oxford energy dissipation spectroscopy (EDS) operated at 20 kV. Transmission electron microscopy (TEM) was acquired from JEOL JEM 2100-F operating at 200 kV.

2.8 Electrochemical characterisation

Electrochemical characterisations were performed using the Biologic potentiostat. CE and RE were similar to those reported in section 2.3 respectively, CN and MO/RGO-S-X@CN served as the WE In three-electrode configuration. The positive three-electrode measurements of all the samples were performed in 2 M KOH. The CV was executed over scan rates ranging from 5 - 100 mV s^{-1} vs Ag/AgCl, The GCDs were run at a specific current of 0.5 – 10 A g^{-1}. Electrochemical impedance spectroscopy (EIS) was performed in an open circuit potential at frequencies ranging from 10 mHz to 100 kHz.

3.0 Results and analysis

3.1 Microstructural characterisation and analysis

Fig. S1 (a-c) (supplementary information), shows low-resolution SEM images of CN synthesized by varying the number of CV cycles at 5 mV s^{-1}. The nanoflake morphology is

maintained even after varying the number of cycles from 3 to 9. Fig S2 (a) and (b) reveal the SEM images respectively of CCBW at low and high magnifications. The morphology displays the porous nature of carbon material. Fig. 2 shows SEM micrographs at low and high magnifications of the produced samples. Fig. 2(a) and (b) display densely packed MO nanospheres while Fig. 2(c) and (d) presents the morphology of CN nanoflakes of about 300 nm in width vertically grown on NF. Fig. 2(e) and (f) display the morphology of MO/RGO-S which confirms the presence of RGO-S nanorods of about 250 nm in length within the samples. Fig 2(g) and (h) illustrate the images of MO/RGO-S@CN, in which the surface is almost completely covered with nanoflakes from cobalt-nickel layered double hydroxide. Fig S3 indicates the HRTEM image of the MO/RGO-S-50@CN composite sample. The structure consists of a shroud of nanoflakes of CN encompassing the nanorod array of RGO-S. This array facilitates ion penetration and enhances redox reaction through the enlargement of the contact area between the electrode material and electrolyte.

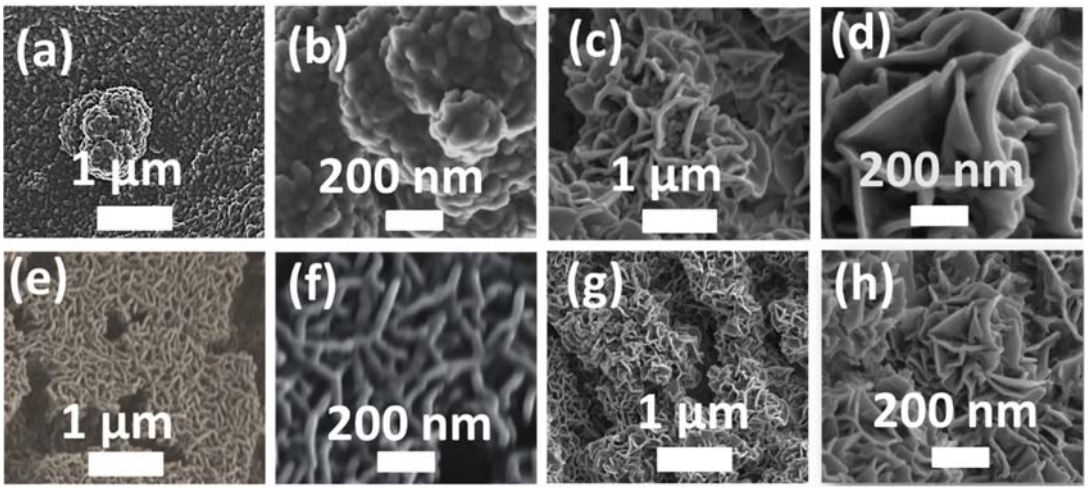

Fig. 2: (a) and (b) low- and high-resolution micrographs respectively of MO, (c) and (d) low- and high-resolution images respectively of CN, (e) and (f) low- and high-resolution images respectively of MO/RGO-S, (g) and (h) low- and high-resolution images respectively of MO/RGO-S-50@CN.

Fig. S4 (a)-(f) show the EDS mapping of the MO/RGO-S-50@CN displaying oxygen, manganese, carbon, nickel, sulphur and cobalt respectively within the material. The images show that the elements are evenly distributed on the sample with Co (5.96 %), Ni (11.03 %), Mn (25.75 %), O (44.78 %) S (0.49 %) and C (11.98 %). From these images, it is evident that the elements are evenly spread in the sample. Fig. S4 (g) shows the spectrum which displays the percentage composition of these elements.

Fig. S5 shows XRD patterns of CN, MO/RGO-S@CN with different RGO-S mass loading and NF. The diffraction peaks at 2θ = 9.7, 19.4, 33.3, 38.2, 47.7, 58.7 and 61.9°, corresponds to the planes (003), (006), (009), (015), (018), (110) and (113) respectively of CN (JCPDS No.14-0191) [29]. The peaks 2θ values of 17.9, 27.6, 28.9, 34.5, 55.4 and 60.3°, corresponds to the planes (101), (112), (103), (211), (312), and (224) respectively of MO (JCPDS No.24-0734) [29]. The 2θ value at 26.5° corresponds to the (002) plane showing the presence of graphitic material and evidence of the incorporation of RGO-S. The amorphous nature of AM is evident in the broad and unclear peaks. These peaks are however overshadowed by the sharp peaks from nickel foam.

Fig. 3 indicates the Raman spectrum of CN, MO/RGO-S-X@CN where X denotes the various mass loading of RGO-S. CN shows the E_{1g} at 479 cm^{-1} which reveals the presence of O-Ni-O and O-Co-O while F_{2g} and A_{1g} at 546 and 673 cm^{-1} respectively reveal the presence of Ni-OH and Co-OH bonds [30]. The peak at 645 cm^{-1} in MO/RGO-S-X@CN relates to the A_{1g} stretching of the Mn-O bond of the Hausmannite spinel [31,32]. The G and D peaks at 1595 and 1354 cm^{-1} respectively confirm the successful integration of RGO-S in the composite's material. The D peak is the k-point phonon of A_{1g} symmetry [33] which can be attributed to the structural defects, edges, or the presence of functional groups. The G peak denotes the in-plane stretching of the sp^2 carbon atom [34]. The Raman in Fig. S6 shows the spectrum of CN samples synthesized by varying the number of CV cycles during the

electrodeposition at 5 mV s^{-1}. The E_{1g} and F_{2g} peaks are present in all the samples while the A_{1g} is also visible for 3 and 9 cycles scan. The A_{1g} peak is most pronounced in the 6 cycle scans presenting the appropriate number of CV cycles scan required for effective deposition of CN samples.

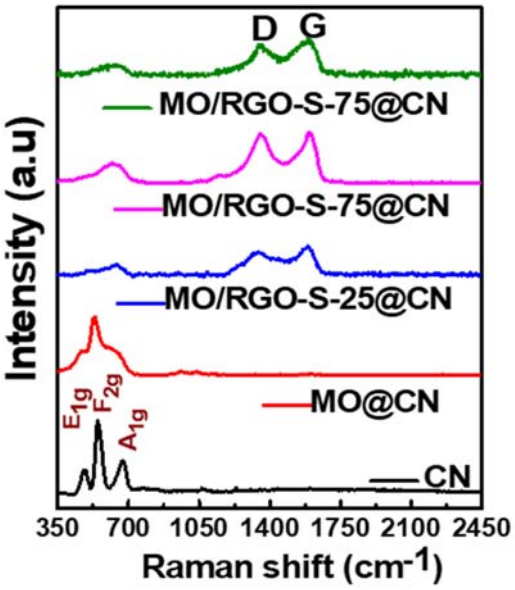

Fig. 3: Raman spectrum for different samples: CN, MO@CN, MO/RGO-S-25@CN, MO/RGO-S-50@CN, MO/RGO-S-75@CN

3.2 Electrochemical performance of the as-synthesized samples

3.2.1 Three-electrode evaluations

Fig S7 shows the CV traces of MO/RGO-S-50@CN at 50 mV s^{-1} using different electrolytes. It's evident that 2 M KOH displays the highest specific current, hence 2 M KOH was selected for further electrochemical tests. Fig. S8 (a) exhibits the CV of the CN samples synthesized at a range of number cycles in 2 M KOH electrolyte. The 6 cycles sample presents the superior current peak which is supported by the GCD in Fig. S8 (b) where the 6 cycles sample has the longest discharge time. Fig. S8 (c) shows that the 6-cycle sample

has the highest specific capacity compared to 3 and 9 cycles at 0.5 A g^{-1}. The EIS Nyquist plot in Fig. S8 (d) shows that the 6-cycles sample has the smallest equivalent series resistance (ESR) and short diffusion length compared to others. The overall electrochemical comparison shown in Fig. S8 reveals an outstanding performance for sample synthesized for 6 cycles, thus, all further electrodeposition of CN on the composites was performed using 6 cycles sample.

Fig. 4 presents the 3-electrode measurements of all different samples using 2 M KOH. Fig. 4 (a) displays the CV at a 50 mV s^{-1} in a voltage range 0 - 0.5 V vs Ag/AgCl. The traces show reduction peaks demonstrating the presence of Faradaic charge storage structure within the material. The reduction peaks are within (0.1-0.3) V vs Ag/AgCl, while in the entire voltage range the oxidation peak is not visible. The lack of prominence in the redox peaks point to pseudocapacitive charge storage mechanism rather than pure Faradaic battery-type charge storage. The MO/RGO-S-50@CN showed the best current response compared to CN, MO@CN, MO/RGO-S-25@CN, and MO/RGO-S-75@CN samples. This may be credited to the enhanced electrical conductivity due to the optimum content of RGO-S in the MO matrix. The manifestation of the Faradaic nature of the layered double hydroxide and spinel is supported by the GCD in Fig. 4 (b) at a specific current of 0.5- A g^{-1}. The slanted plateaux support the redox mechanisms shown in the CVs in Fig. 4(a) and the lengthiest discharge time is observed in MO/RGO-S-50@CN in coherence with the highest current peak in the CV trace. Fig. 4 (c) indicates the specific capacity versus specific current at 0.5 A g^{-1} with the MO/RGO-S-50@CN sample showing the highest specific capacities for all specific currents reported. The specific capacity (Q_S) is calculated using equation [35] (6):

$$Q_S\ (mAh\ g^{-1}) = \frac{1}{3.6} \times I_S \Delta t \qquad (6)$$

where, I_S denotes the specific current (A g^{-1}), and Δt represents the time of discharge (s). All samples show high specific capacities and rate capability which could be due to the synergistic effects of multi-components [29]. The rate capabilities at 10 A g^{-1} are 84, 51, 71, 62 and 35% for CN, MO@CN, MO/RGO-S-25@CN, MO/RGO-S-50@CN and MO/RGO-S-75@CN, respectively. The high rate capability is due to the high electrical conductivity for the samples [36]. However, the lower rate capability of MO/RGO-S-75@CN can be attributed to the increased contact resistance due to the large mass loading of RGO-S in the composite [37]. Fig. 4 (d) shows the Nyquist plot to analyse the electrical conductivity and kinetics of charges of all samples. The ESR magnitudes which correspond to the intercept of the x-axis, as shown in the insert at high frequency in Fig. 3(d) are 1.32, 1.46, 1.58, 1.39 and 2.04 Ω for CN, MO@CN, MO/RGO-S-25@CN, MO/RGO-S-50@CN and MO/RGO-S-75@CN, respectively. These small values indicate the electrolyte's low ionic resistance, minimal contact resistance of the AM and current collector with the better conductivity of the AM. The small contact resistance of NF with the AM is attributed to the strong adhesive forces of the electrodeposition method. The diameters of the semi-circles which are depressed by the constant phase element (CPE) are very short for all the samples signifying low charge transfer resistance. Fig. 4 (e) shows the cyclic stability of up to 5, 000 GCD cycles at 6 A g^{-1}. The coulombic efficiency (η) is calculated using equation (7):

$$\eta = \frac{t_D}{t_C} \times 100\ \% \tag{7}$$

where t_C and t_D are the times (s) for charge and discharge respectively. Coulombic efficiency of CN, MO@CN, MO/RGO-S-25@CN, MO/RGO-S-50@CN, MO/RGO-S-75@CN were 99.8, 99.7, 99.5, 99.9 and 97.4%, respectively which are almost 100% which was is expected of supercapacitors. All the samples except the MO/RGO-S-75@CN had an excellent coulombic efficiency of at least 99.5 %. The decrease of the efficiency of MO/RGO-S-

75@CN is due to excess content of RGO-S in the sample causing saturation. The excellent performance presented by other samples shows good redox reversibility which is attributed to the high chemical stability of MO and excellent structural design of the electrodeposition synthesis. The increased redox reactivity and high adsorption property of MO enhanced the phenomenal electrochemical attributes of the composite samples. The composites have a dominant Faradaic charge storage mechanism due to the presence of CN and MO and it is more prominent than the EDLC storage mechanism from RGO-S. The synergistic effect of both storage mechanisms helps to considerably enhance the electrochemical performance of the composite material as compared to individual electrode materials. The superior coulombic efficiency of 99.9 % for MO/RGO-S-50@CN is due to the structural stability owing to the optimum amount of RGO-S in the sample. From Fig. 4 it is evident that the electrochemical execution of MO/RGO-S-50@CN surpasses all the other samples.

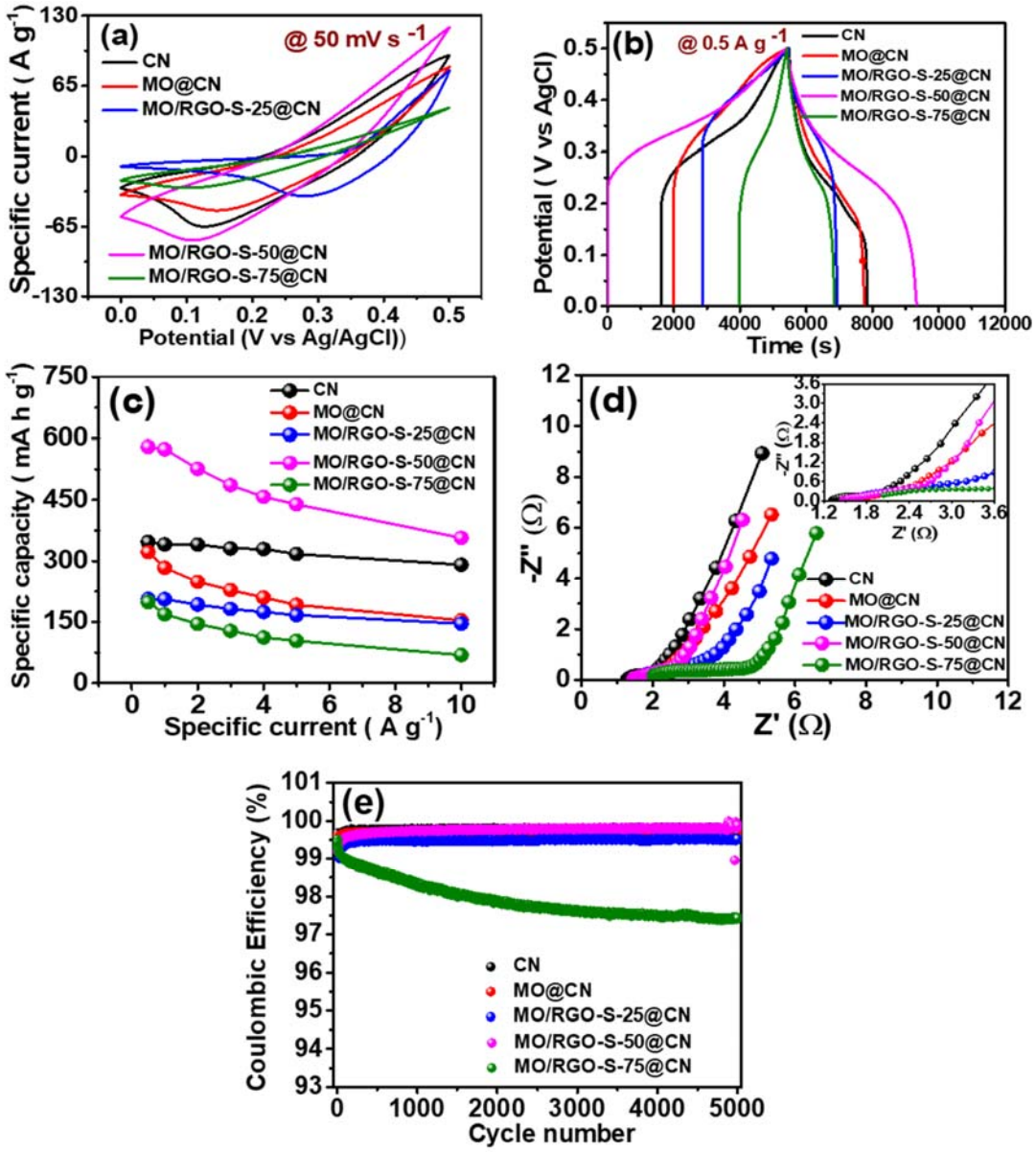

Fig. 4: (a) The CV traces, (b) The GCD traces, (c) specific capacity vs specific current, (d) EIS Nyquist plot, (e) Coulombic efficiency of CN, MO@CN, MO/RGO-S-25@CN, MO/RGO-S-50@CN and MO/RGO-S-75@CN, respectively.

Fig. 5 summarises the electrochemical functioning of the best (optimal) sample MO/RGO-S-50@CN. Fig. 5 (a) indicates the CV curves in a voltage range of 0 - 0.5 V vs Ag/AgCl with scan rates range 5 - 100 mV s^{-1}. There are pairs of reduction and oxidation peaks for

all the scan rates. However, at higher scan rates of 50 and 100 mV $s^{-1,}$ the oxidation peaks are merely invisible. This is due to the increase in charge diffusion polarisation in the electrode material with scan rate which leads to the reduction in the reversibility of the redox process. The peaks are due to the following electrochemical reactions:

$$Ni(OH)_2 + OH^- \rightleftharpoons NiOOH + H_2O + e^- \quad (8)$$

$$Co(OH)_2 + OH^- \rightleftharpoons CoOOH + H_2O + e^- \quad (9)$$

$$\mathrm{Co}OOH + OH^- \rightleftharpoons CoO_2 + H_2O + e^- \quad (10)$$

Fig 5(b) presents the GCD at a specific current range from 0.5 - 10 A g^{-1}, the absence of a well-pronounced plateau indicates pseudocapacitive behaviour instead of a pure battery type storage mechanism. Fig 5(c) displays the capacity retention and coulombic efficiency during 5 000 GCD cycles at 6 A g^{-1}. The high-capacity retention of 86.5 % and a coulombic efficiency of 99.9 % is due to the strong adhesion between the current collector and electrode material. This is also attributed to electrodeposition synthesis and the mechanical stability from the inclusion of RGO-S in the composite material. Therefore, MO/RGO-S-50@CN was preferred for use as the positive electrode for fabrication of the device due to the superior electrochemical performance displayed by this sample compared to the other electrodes.

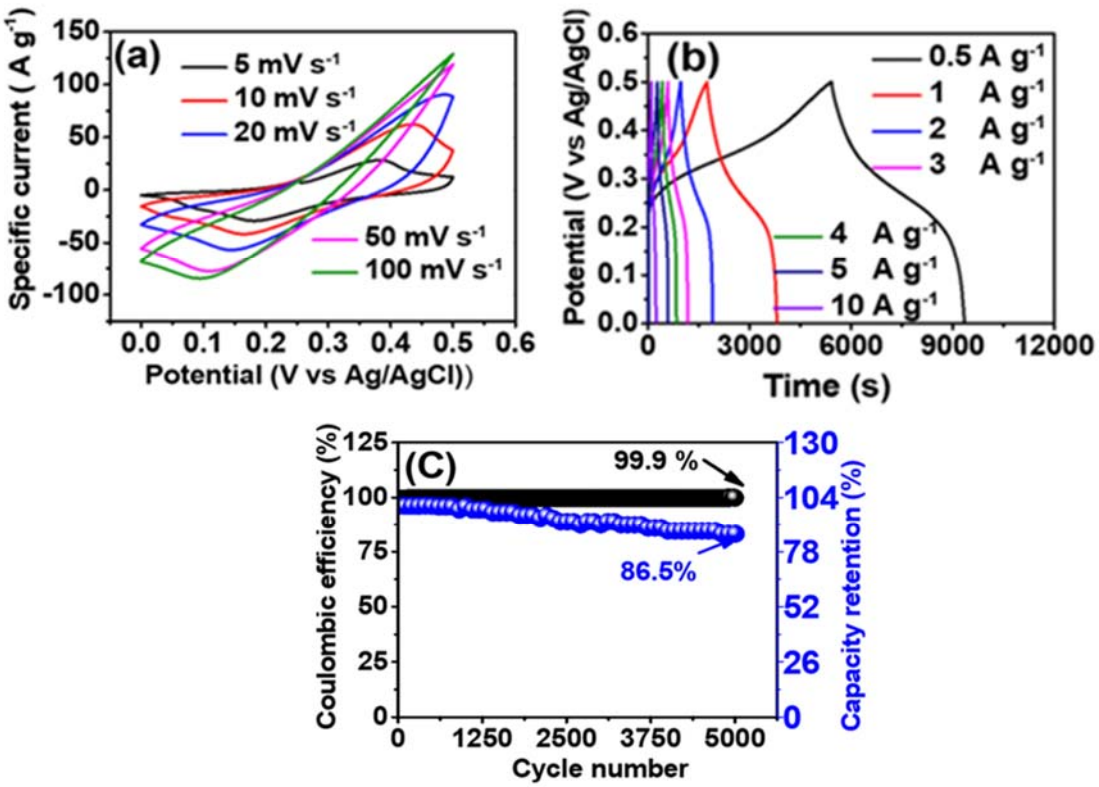

Fig. 5: (a) CV traces, (b) GCD traces and (d) Capacity retention and coulombic efficiency for MO/RGO-S-50@CN sample.

Table 1 shows a comparison of electrochemical performance of LDH electrode materials synthesized using various methods which were reported beforehand (the units were all converted to mAh g^{-1} for comparison). The electrode in this work produced the highest specific capacity of 582.1 mAh g^{-1} at 0.5 A g^{-1} and excellent capacity retention of 86.5 % at 5000 GCD cycles at 6 A g^{-1}. The synthesized electrode revealed higher performance in a three-electrode configuration ahead of other related materials appearing in the recently published studies as displayed in Table 1. From the table, we observe various synthesis methods for cobalt-nickel based electrodes. We observe slightly higher specific capacities from electrodes synthesized via the electrodeposition methods compared to other synthesis methods. The composites of the LDH with other materials leads to better electrochemical

performance. The electrode materials in this work are superior and this may be as a result of the presence of a carbon material that is absent in other electrodes reported in the literature.

Table 1: Electrochemical performance of recently reported LDHs in a three-electrode system.

Material	Synthesis method	Capacity ($mAh\ g^{-1}$)	Capacity retention (cycles)	Reference
Ni-Co LDHs	Electrodeposition	287 (1 $A\ g^{-1}$)	81.8% (3000)	[38]
Ni-Co LDH	Hydrothermal	217 (6 Ag^{-1})	86% (1000)	[39]
P@NiCo LDHs	Co-precipitation	149 (1 Ag^{-1})	55.9% (5000)	[40]
Ni-Co LDH/CFC	Electrodeposition	235 (1 Ag^{-1})	82.9 % (5000)	[41]
FeNiP@CoNi-LDH	Hydrothermal	285 (1 Ag^{-1})	70.4% (5000)	[42]
CoNi-LDH67	Co-precipitation	183 (1 Ag^{-1})	77.14 % (5000)	[43]
MO/RGO-S-50@CN	**Electrodeposition**	**582.1 (0.5 A g^{-1})**	**86.5% (5000)**	**This work**

3.2.2 Electrochemical properties of the asymmetric supercapacitor

To evaluate the actual performance of the synthesized electrode, an asymmetric device MO/RGO-S-50@CN//CCBW was made using MO/RGO-S-50@CN as a positive electrode and CCBW as a negative electrode with 2 M KOH electrolyte. To attain charge balance of the electrodes, the mass ratio of the negative and positive electrode materials was obtained using mass balance equation [44]:

$$\frac{m_-}{m_+} = 3.6\frac{Q_{S+}}{C_{s-} \times V_{S_-}} \tag{11}$$

here m_- and m_+ denotes the negative and positive electrode masses (mg), Q_{S+} is the positive electrode specific capacity (mAh g^{-1}), C_{S-} is the negative electrode's specific capacitance (F g^{-1}) and V_{S-} is the potential (V) of the negative electrode.

The total mass of AM in the device was 5.0 mg/cm^2 and the calculated ratio m-/m+ was 10:1. Fig. 6 (a) indicates the CV curves for the negative and positive electrodes at 50 mV s^{-1} in which the CCBW manifests a rectangular-like EDLC behaviour within the potential windows of -0.9 to 0 V vs Ag/AgCl, while MO/RGO-S-50@CN shows a Faradaic behaviour in the positive voltage range of 0 to 5 V vs Ag/AgCl. Fig. 6 (b) displays the CV of the device at 5 - 100 mV s^{-1} scan rate whereby the redox crests are manifested even at a large scan rate of 100 mV s^{-1} proving great rate performance for the device. Fig. 6 (c) presents the GCD at specific currents ranging from 0.5 to 10 A g^{-1} with non-linear traces that are coherent with the Faradaic charge storage mechanism [45]. Fig. 6 (d) represents specific capacity vs specific current with the largest specific capacity of 55.0 mAh g^{-1} at 0.5 A g^{-1}. Fig. 6 (e) demonstrates coulombic efficiency and capacity retention variation with cycle number. The device retains a coulombic efficiency of 99.7 % and capacity retention of 85.1% at 10,000 GCD cycles performed at 6 A g^{-1}. This performance is influenced by the absence of polymeric binders in the positive electrode which contributes to these high stability values [46]. The insert in Fig. 6 (e) shows 5 light-emitting diodes (LEDs) lighted by two MO/RGO-S-50@CN//CCBW devices connected in parallel after 10,000 cycles of stability test. The specific energy (E_s) is calculated using the following equation [47]:

$$E_s\ (Wh\ kg^{-1}) = \frac{I_s}{3.6} \int V(t)dt \qquad (12)$$

where $\int V(t)dt$ depicts the integral (Vs) and I_S is the specific current (A g^{-1}) of the GCD curve. The specific power (P_S) is obtained from the following expression [48]:

$$P_s\ (W\ kg^{-1}) = 3600 \times \frac{Es}{\Delta t} \quad (13)$$

where Δt is the time of discharge (s).

The device MO/RGO-S-50@CN//CCBW in this work produced a specific energy of 56.0 Wh kg^{-1} at a specific current of 0.5 A g^{-1} which corresponds to a specific power of 515.0 W kg^{-1}. Fig. 6 (f) displays the Ragone plot associating the specific energy and power of this work to other similar devices on cobalt-nickel layered double hydroxide/spinel composites in the literature. The plot shows that the specific energy and power of the device in this work is mostly better than other reported related work [18,40,49–52]. The maximum power is transferred when the resistance of the load is equal to the ESR. The maximum specific power P_{MAX} of the device is obtained by employing equation [53] :

$$P_{MAX}\ (kW\ kg^{-1}) = \frac{V^2}{4m \times R_S} \quad (14)$$

where m is the mass (g) of AM in the device, V is the cell potential (V), and R_S (Ω) is the ESR of the device. The device produces a maximum specific power of 139.9 kW kg^{-1}.

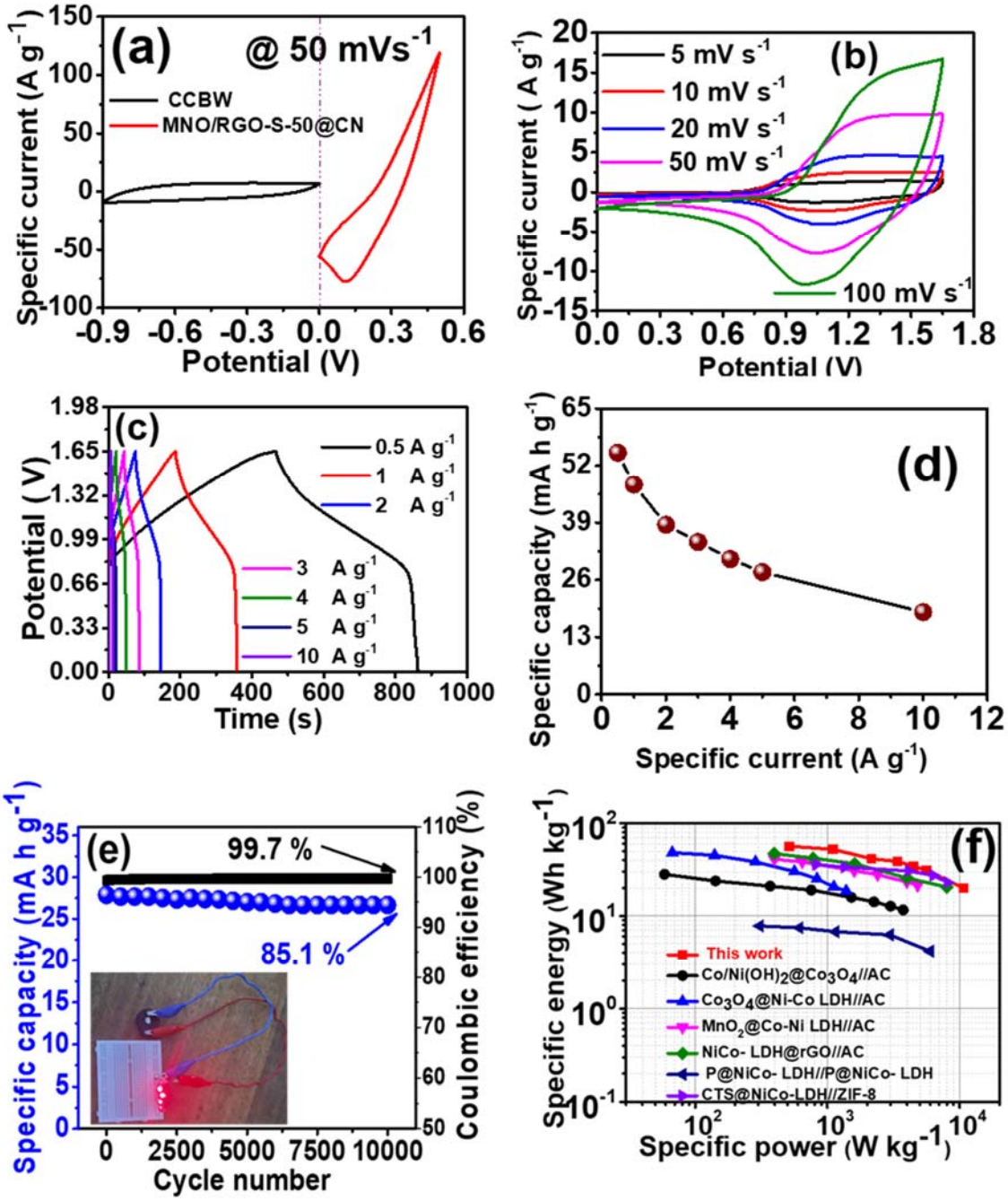

Fig. 6 (a): CV traces of the negative and positive electrode at 50 mV s^{-1}, (b) CV traces of the device at different scan rates, (c) GCD traces at a range of specific currents, (d) specific capacity vs specific current, (e) cyclic stability and capacity retention versus cycle number with an insert being 5 LED lighted by two asymmetric devices in parallel, and (f) Ragone plot of MO/RGO-S-50@CN//CCBW device, respectively.

Table 2 displays a contrast of the electrochemical characteristics of devices previously reported which are based on CN materials. The device in this work produced a huge specific energy of 56 Wh kg^{-1} at a cell potential of 1.65 V.

Table 2: Electrochemical performance of earlier reported LDHs-based electrode material in a device.

Device	**Electrolyte**	**Cell potential (V)**	**E_S (Wh kg^{1})**	**P_S (W kg^{1})**	**Ref.**
$NiCo_2O_4$@NiCo-LDH//NGH	2 M KOH	1.55	50.7	773.5	[54]
NiCoP/NiCo-OH//PC	6 M KOH	1.6	34	775	[55]
Ni-Co LDH/CFC//rGO/NF	6 M KOH	1.6	37	800	[41]
CoNi LDH-6//EWC-2 ASC	2 M KOH	1.7	51.1	1700	[56]
MnO_2@ Co-Ni LDH//AC	1 M KOH	1.6	40.9	400	[50]
MCS@CN LDH//N-rGO	6 M KOH	1.6	48.8	800	[57]
MO/RGO-S@CN//CCBW	**2 M KOH**	**1.65**	**56**	**515**	**This work**

Fig. 7 (a) illustrates the Nyquist plot of the device displaying the experimental results together with the fitting line. The insert shows the equivalent circuit used to fit data. The device presented a meagre value of ESR denoted as R_S of 1.059 Ω which is attributed to minimal contact resistance at the AM/current collector interface and electrolyte ions/electrode materials interface. The equivalent circuit shows the charge transfer resistance (R_{CT}) of 4.31 Ω which demonstrates the occurrence of Faradaic reactions. R_{CT} is parallel to the CPE (Q), which causes the semi-circle to be depressed such that the centre is below the real impedance axes. The resistance due to leakage currents, R_L which has a value of 1.69 Ω, causes the plot curve to bend away from the imaginary impedance axes causing the magnitude of the phase angle to be less than 90°. The Warburg-frequency (Z_w) also

causes the slope to deviate from the imaginary impedance axes in the low frequency section, this impedes ion diffusion to the electrode surface. Fig. 7 (b) shows the EIS Nyquist plot before cycling and after 10,000 GCD cycles. The Rs decreases to 0.980 Ω after 10,000 cycles which indicates a decrease in the resistance at electrolyte-electrode plotline and the reduction in AM-current collector contact resistance. However, the slope of the plot line after the stability test indicates a rise in the diffusion resistance on the electrode-electrolyte interface due to the water molecules in the electrolyte decomposing [57]. Fig. 7(c) is the Bode plot showing the variation of phase angle with frequency in which the phase angle for our device at the low frequency region is -71°. This value which is close to -90° indicates the presence of capacitive behaviour in the device. Fig. 7 (d) shows the variation of imaginary and real capacitance ($C''(\omega)$ and $C'(\omega)$) with frequency. The imaginary and real capacitances are calculated from the equation expressed below [58]:

$$Z'(\omega) = 2\pi f C''(\omega)|Z(\omega)| \tag{15}$$

$$Z^{''}(\omega) = 2\pi f C^{'}(\omega)|Z(\omega)| \tag{16}$$

where ω is the angular frequency (rad s^{-1}) which is given by $\omega = 2\pi f$, f depicts the frequency (Hz), and Z represents the impedance (Ω). The real capacitance C′(ω) is the capacitance (F) of the device which is accessible and transferred and it denotes a maximum value of 0.46 F at low frequency as shown in Fig. 7 (d). The imaginary component of the capacitance C′′(ω) correspond to the energy lost by the electrodes through irreversible processes. The C′′(ω) has a peak maximum value of 0.44 F at 0.05 Hz. This corresponds to the relaxation time τ of 3.2 s obtained using 2πfτ = 1. This demonstrates that the MO/RGO-S-50@CN//CCBW device can be fully charged quickly with 3.2 s.

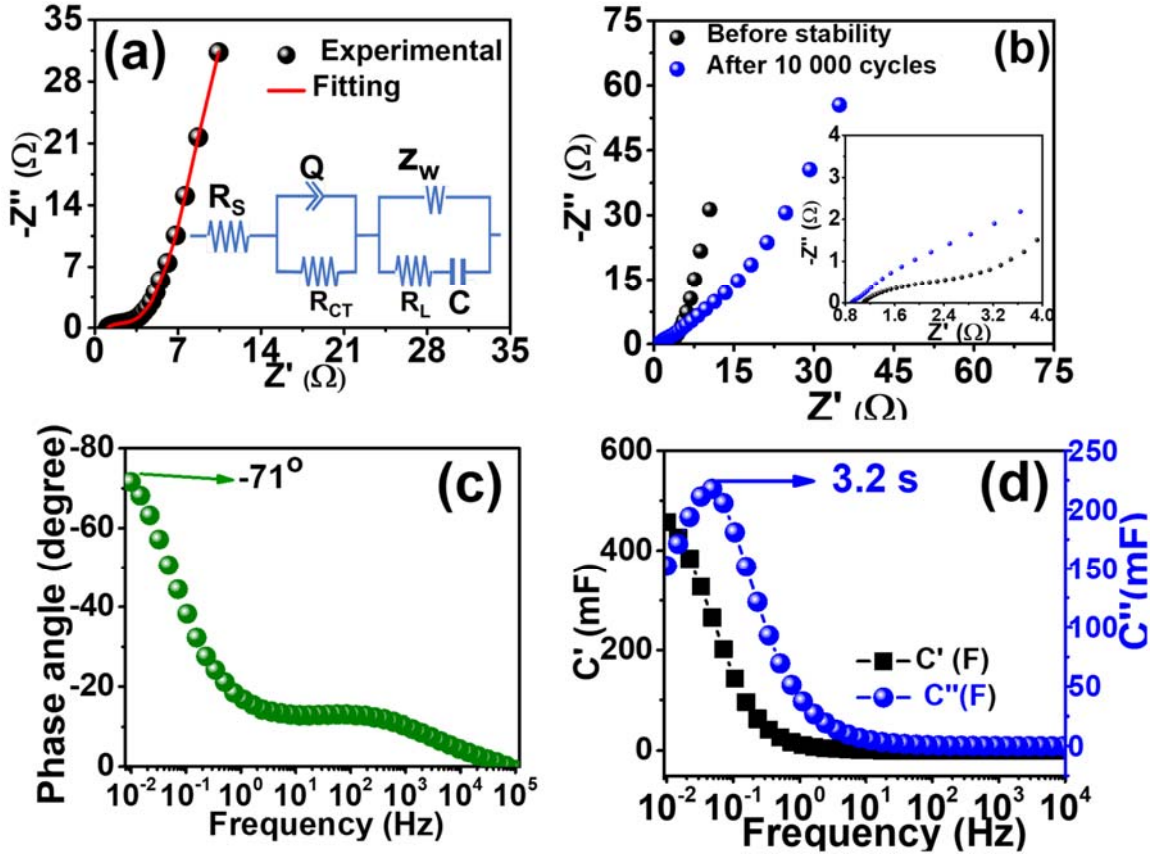

Fig. 7: (a) Nyquist plot of the experimental data with the fitting curve and an equivalent circuit, (b) Nyquist plot before and after cycling stability with insert, (c) Bode plot, and (d) Imaginary and real capacitance vs frequency.

4.0 Conclusion

MO/RGO-S-X@CN was produced through a two-step electrodeposition method. The optimized electrode material (MO/RGO-S-50@CN) produced an outstanding performance with an excellent specific capacity of 582.1 mAh g^{-1} at 0.5 A g^{-1}. The electrode further demonstrated a coulombic efficiency of 99.9 % after 5 000 GCD cycles at 6 A g^{-1}. A device was fabricated with activated carbon from cooked chicken bone waste (CCBW) as the negative electrode and the synthesized material (MO/RGO-S-50@CN) as the positive electrode. The MO/RGO-S-50@CN//CCBW device produced a specific energy of 56.0 Wh

kg^{-1} at 0.5 A g^{-1} with an equivalent specific power of 515.0 W kg^{-1}. The device also presented a coulombic efficiency of 99.7 % at 10 000 GCD cycles at 6 A g^{-1} with a capacity retention of 85.1%. This outstanding electrochemical performance of the device enables it to be incorporated in energy storage systems for renewable energy.

Acknowledgements

This research was sustained by the South African Research Chairs Initiative (SARChI) of the Department of Science and Technology and the National Research Foundation (NRF) South Africa (Grant number. 61056). Any idea, discovery, recommendation, and conclusions in this work are the that of author(s) and NRF does not take any liability in this regard. Gift Rutavi recognises the support from NRF through SARChI in Carbon materials.

References:

1. Relva, S. G. *et al.* Enhancing developing countries' transition to a low-carbon electricity sector. *Energy* **220**, (2021).
2. Ji, Y. *et al.* Carbon aerogels with mutual support structures constructed by hybrid hydrogels: Robust energy storage materials. *Mater. Today Commun.* **25**, 101444 (2020).
3. Chodankar, N. R., Selvaraj, S., Ji, S. H., Kwon, Y. & Kim, D. H. Interface-Engineered Nickel Cobaltite Nanowires through NiO Atomic Layer Deposition and Nitrogen Plasma for High-Energy, Long-Cycle-Life Foldable All-Solid-State Supercapacitors. *Small* **15**, 1–12 (2019).
4. Sharma, P. & Kumar, V. Current Technology of Supercapacitors: A Review. *J. Electron. Mater.* **49**, 3520–3532 (2020).

5. Yu, F. *et al.* Design and synthesis of electrode materials with both battery-type and capacitive charge storage. *Energy Storage Mater.* **22**, 235–255 (2019).

6. Zou, Q. *et al.* Supercritical ethanol deposition of Ni(OH)2 nanosheets on carbon cloth for flexible solid-state asymmetric supercapacitor electrode. *J. Supercrit. Fluids* **159**, 104774 (2020).

7. Wang, D., Li, J., Zhao, Y., Xu, H. & Zhao, J. Bifunctional Cu2S–Co(OH)2 nanotube array/Cu foam electrocatalyst for overall water splitting. *Electrochim. Acta* **316**, 8–18 (2019).

8. Hu, P., Liu, Y., Song, J., Song, X. & Wu, X. Transition metal oxide@hydroxide assemblies as electrode materials for asymmetric hybrid capacitors with excellent cycling stabilities. *RSC Adv.* **9**, 32510–32516 (2019).

9. Tomboc, G. M. *et al.* Hybrid layered double hydroxides as multifunctional nanomaterials for overall water splitting and supercapacitor applications. *J. Mater. Chem. A* **9**, 4528–4557 (2021).

10. Tang, Y. *et al.* A comparative study and optimization of corrosion resistance of ZnAl layered double hydroxides films intercalated with different anions on AZ31 Mg alloys. *Surf. Coatings Technol.* **358**, 594–603 (2019).

11. Manohara, G. V., Norris, D., Maroto-Valer, M. M. & Garcia, S. Acetate intercalated Mg-Al layered double hydroxides (LDHs) through modified amide hydrolysis: a new route to synthesize novel mixed metal oxides (MMOs) for CO2capture. *Dalt. Trans.* **50**, 7474–7483 (2021).

12. Arrabito, G. *et al.* Layered double hydroxides: A toolbox for chemistry and biology. *Crystals* **9**, (2019).

13. Li, C. *et al.* Ni dopping Co2Al ternary layered double hydroxides for improving electrochemical performance of high-performance hybrid supercapacitors. *Appl.*

Surf. Sci. **536**, 147780 (2021).

14. Zhao, Z., Kou, K. & Wu, H. 2-Methylimidazole-mediated hierarchical Co3O4/N-doped carbon/short-carbon-fiber composite as high-performance electromagnetic wave absorber. *J. Colloid Interface Sci.* **574**, 1–10 (2020).
15. Enhtuwshin, E. *et al.* Ni-Fe-Cu-layered double hydroxides as high-performance electrocatalysts for alkaline water oxidation. *Int. J. Energy Res.* **45**, 15312–15322 (2021).
16. Yan, Z. *et al.* Electrodeposition of (hydro)oxides for an oxygen evolution electrode. *Chem. Sci.* **11**, 10614–10625 (2020).
17. Mbugua, N. S. *et al.* Electrochemical deposition of Ni, NiCo Alloy and NiCo-ceramic composite coatings-A critical review. *Materials (Basel).* **13**, (2020).
18. Bao, Y. *et al.* A controllable top-down etching and in-situ oxidizing strategy: metal-organic frameworks derived α-Co/Ni(OH)2@Co3O4 hollow nanocages for enhanced supercapacitor performance. *Appl. Surf. Sci.* **504**, 144395 (2020).
19. Sherryna, A. & Tahir, M. Recent developments in layered double hydroxide structures with their role in promoting photocatalytic hydrogen production: A comprehensive review. *Int. J. Energy Res.* 1–48 (2021) doi:10.1002/er.7335.
20. Kashale, A. A. *et al.* Binder-free heterostructured NiFe2O4/NiFe LDH nanosheet composite electrocatalysts for oxygen evolution reactions. *ACS Appl. Energy Mater.* **3**, 10831–10840 (2020).
21. Zhao, X. *et al.* Two-dimensional Spinel Structured Co-based Materials for High Performance Supercapacitors: A Critical Review. *Chem. Eng. J.* **387**, 124081 (2020).
22. Wang, Z. *et al.* Establishing highly-efficient surface faradaic reaction in flower-like NiCo 2 O 4 nano-/micro-structures for next-generation supercapacitors.

Electrochim. Acta **307**, 302–309 (2019).

23. Chen, J. *et al.* Graphene-wrapped MnCO3/Mn3O4 nanocomposite as an advanced anode material for lithium-ion batteries: synergistic effect and electrochemical performances. *J. Mater. Sci. Technol.* **99**, 9–17 (2021).

24. Song, B., Cerkez, E. B., Elzinga, E. J. & Kim, B. Effects of Ni incorporation on the reactivity and stability of hausmannite (Mn3O4): Environmental implications for Mn, Ni, and As solubility and cycling. *Chem. Geol.* **558**, 119862 (2020).

25. Bhagwan, J., Krishna, B. N. V. & Yu, J. S. Template and sol-gel routed CoMn2O4 nanofibers for supercapacitor applications. *Int. J. Energy Res.* **45**, 19413–19422 (2021).

26. Singh, A., Ojha, S. K. & Ojha, A. K. Facile synthesis of porous nanostructures of NiCo2O4 grown on rGO sheet for high performance supercapacitors. *Synth. Met.* **259**, 116215 (2020).

27. Tarimo, D. J., Oyedotun, K. O., Mirghni, A. A. & Manyala, N. Sulphur-reduced graphene oxide composite with improved electrochemical performance for supercapacitor applications. *Int. J. Hydrogen Energy* **45**, 13189–13201 (2020).

28. Pan, G. T., Chong, S., Yang, T. C. K. & Huang, C. M. Electrodeposited porous mn1.5co1.5o4/ni composite electrodes for high-voltage asymmetric supercapacitors. *Materials (Basel).* **10**, 1–12 (2017).

29. Zhao, N. *et al.* Preparation of partially-cladding NiCo-LDH/Mn3O4 composite by electrodeposition route and its excellent supercapacitor performance. *J. Alloys Compd.* **796**, 111–119 (2019).

30. Zhu, Y. *et al.* Core-branched NiCo2S4@CoNi-LDH heterostructure as advanced electrode with superior energy storage performance. *Chem. Eng. J.* **383**, 123206 (2020).

31. Li, Q. *et al.* Performance of chemically synthesized Mn3O4/rGO nanocomposite for electrochemical supercapacitor: a cost-effective high-performance electrode. *Nanotechnology* **31**, (2020).

32. T. V. M., S., Kisoo, Y. & Kim, J. Temperature-dependent synthesis of Mn3O4 nanostructures by microwave irradiation method for high-performance supercapacitors. *Int. J. Energy Res.* **46**, 1683–1692 (2022).

33. Maphiri, V. M. *et al.* Novel thermally reduced graphene oxide microsupercapacitor fabricated via mask—free axidraw direct writing. *Nanomaterials* **11**, (2021).

34. Hiremath, V., Lim, A. C. & Seo, J. G. Highly porous honeycomb-like activated carbon derived using cellulose pulp for symmetric supercapacitors. *Int. J. Energy Res.* **45**, 4385–4395 (2021).

35. Kitenge, V. N. *et al.* Enhancing the electrochemical properties of a nickel–cobalt-manganese ternary hydroxide electrode using graphene foam for supercapacitors applications. *Mater. Renew. Sustain. Energy* **10**, 1–16 (2021).

36. Zhang, L. & Shi, G. Preparation of highly conductive graphene hydrogels for fabricating supercapacitors with high rate capability. *J. Phys. Chem. C* **115**, 17206–17212 (2011).

37. Han, H. *et al.* Dominant factors governing the rate capability of a TiO 2 nanotube anode for high power lithium ion batteries. *ACS Nano* **6**, 8308–8315 (2012).

38. Ju, A. *et al.* Electrodeposition of Ultrathin Nanosheets of Nickel-Cobalt Double Hydroxides with Layered Structure for Improved Supercapacitor Performance. *Int. J. Electrochem. Sci.* **16**, 1–15 (2021).

39. Pu, J., Tong, Y., Wang, S., Sheng, E. & Wang, Z. Nickel-cobalt hydroxide nanosheets arrays on Ni foam for pseudocapacitor applications. *J. Power Sources* **250**, 250–256 (2014).

40. Wang, G., Li, Y., Zhao, T. & Jin, Z. Phosphatized mild-prepared-NiCo LDHs cabbage-like spheres exhibit excellent performance as a supercapacitor electrode. *New J. Chem.* **45**, 251–261 (2021).

41. Li, Y. *et al.* Ultrathin Ni–Co LDH nanosheets grown on carbon fiber cloth via electrodeposition for high-performance supercapacitors. *J. Mater. Sci. Mater. Electron.* **30**, 13360–13371 (2019).

42. Wan, L. *et al.* Construction of FeNiP@CoNi-layered double hydroxide hybrid nanosheets on carbon cloth for high energy asymmetric supercapacitors. *J. Power Sources* **465**, (2020).

43. Tahir, M. U. *et al.* Room temperature and aqueous synthesis of bimetallic ZIF derived CoNi layered double hydroxides and their applications in asymmetric supercapacitors. *J. Colloid Interface Sci.* **579**, 195–204 (2020).

44. Mahmoud, B. A., Mirghni, A. A., Oyedotun, K. O., Fasakin, O. & Manyala, N. Nanoplatelets ammonium nickel-cobalt phosphate graphene foam composite as novel electrode material for hybrid supercapacitors. *J. Alloys Compd.* **883**, 160897 (2021).

45. Pallavolu, M. R., Gaddam, N., Banerjee, A. N., Nallapureddy, R. R. & Joo, S. W. Superior energy-power performance of N-doped carbon nano-onions-based asymmetric and symmetric supercapacitor devices. *Int. J. Energy Res.* 1234–1249 (2021) doi:10.1002/er.7242.

46. Sun, C., Li, X., Cai, Z. & Ge, F. Carbonized cotton fabric in-situ electrodeposition polypyrrole as high-performance flexible electrode for wearable supercapacitor. *Electrochim. Acta* **296**, 617–626 (2019).

47. Tarimo, D. J. *et al.* Enhanced electrochemical performance of supercapattery derived from sulphur-reduced graphene oxide/cobalt oxide composite and activated

carbon from peanut shells. *Int. J. Hydrogen Energy* **45**, 33059–33075 (2020).

48. Mirghni, A. A. *et al.* High-performance bimetallic Ni-Mn phosphate hybridized with 3-D graphene foam for novel hybrid supercapacitors. *J. Energy Storage* **31**, 101584 (2020).

49. Han, D. *et al.* Co3O4 nanowire@ultrathin Ni-Co layered double hydroxide core-shell arrays with vertical transfer channel for high-performance supercapacitor. *J. Electroanal. Chem.* **859**, (2020).

50. Luo, H. *et al.* Hierarchical design of hollow Co-Ni LDH nanocages strung by MnO2 nanowire with enhanced pseudocapacitive properties. *Energy Storage Mater.* **19**, 370–378 (2019).

51. Zhu, Y. *et al.* Core-branched NiCo2S4@CoNi-LDH heterostructure as advanced electrode with superior energy storage performance. *Chem. Eng. J.* **383**, 123206 (2020).

52. Long, D. *et al.* A facile and large-scale synthesis of NiCo-LDHs@rGO composite for high performance asymmetric supercapacitors. *J. Alloys Compd.* **805**, 1096–1105 (2019).

53. Iqbal, M. Z., Faisal, M. M. & Ali, S. R. Integration of supercapacitors and batteries towards high-performance hybrid energy storage devices. *Int. J. Energy Res.* **45**, 1449–1479 (2021).

54. Acharya, J., Park, M., Ko, T. H. & Kim, B. Leaf-like integrated hierarchical NiCo2O4 nanorods@Ni-Co-LDH nanosheets electrodes for high-rate asymmetric supercapacitors. *J. Alloys Compd.* **884**, 161165 (2021).

55. Li, X. *et al.* Cactus-Like NiCoP/NiCo-OH 3D Architecture with Tunable Composition for High-Performance Electrochemical Capacitors. *Adv. Funct. Mater.* **28**, 1–10 (2018).

56. Chu, H. *et al.* Solvothermal synthesis of cobalt nickel layered double hydroxides with a three-dimensional nano-petal structure for high-performance supercapacitors. *Sustain. Energy Fuels* **4**, 337–346 (2019).

57. Liang, H. *et al.* A free-standing manganese cobalt sulfide@cobalt nickel layered double hydroxide core-shell heterostructure for an asymmetric supercapacitor. *Dalt. Trans.* **49**, 196–202 (2019).

58. Rantho, M. N., Madito, M. J., Ochai-Ejeh, F. O. & Manyala, N. Asymmetric supercapacitor based on vanadium disulfide nanosheets as a cathode and carbonized iron cations adsorbed onto polyaniline as an anode. *Electrochim. Acta* **260**, 11–23 (2018).